



Dynamic modeling of cutting force and surface generation in ultra-precision diamond cutting with microwavy profile effect

Sujuan Wang^{1,3} · Zhenhong Lu¹ · Bowen Hu¹ · Suet To² · Wenyan Tang³

Received: 13 March 2024 / Accepted: 7 August 2024 / Published online: 24 August 2024
© The Author(s), under exclusive licence to Springer-Verlag London Ltd., part of Springer Nature 2024

Abstract

The ultra-precision diamond cutting (UPDC) employs larger cutting parameters in half-finishing process to improve machining efficiency, which introduces microwavy profile to the unmachined surface of finishing process with microscale cutting parameters. The paper makes theoretical and experimental investigations on the microwavy profile effect on cutting process and surface generation in UPDC. The influence of microwavy profile on the surface being machined is considered in diamond cutting process by studying its effect on the instantaneous cutting depth, shear angle, stress, and effective rake angle to build dynamic force model. A new dynamic surface generation model is developed by adding the wavy profile effect and workpiece material properties. The simulated surface profiles in diamond single cutting of different workpiece materials meet well with the experimental ones under different wavy profile patterns. Further studies are conducted to build turning force model and surface profile prediction model for single point diamond turning (SPDT) by adding the diamond-turned microtopography effect on the instantaneous cutting depth. Diamond single cutting experiment and diamond turning experiment are conducted to verify the developed dynamic models, which indicates that the predicted results including cutting force and surface profiles agree well with the experimental results.

Keywords Ultra-precision diamond cutting · Microwavy profile · Cutting force · Surface generation

1 Introduction

Ultra-precision diamond cutting (UPDC) is a promising machining technique for realizing ultra-smooth surface of different kinds of materials in optical, electronic and mechanical components [1]. The ultra-precision cutting (UPC) was firstly studied in the 1960s with the advent of demands in advanced science and technology for energy, computer, electronics, and defense application. In the 1980s, the developments of highly advanced machine tools with

sophisticated metrology and control and of diamond tools of reliable quality makes UPC to begin its extended industrial use for manufacturing of aluminum scanner mirrors, aluminum substrate drums in photo copying machines and aluminum substrates for computer memory disks [2]. After that, more and more applications are found for UPDC in different regions and for different types of materials, such as hard and brittle materials.

All these applications of UPDC require high geometric accuracy and surface roughness, therefore the technique relies on an extremely high fidelity in the transfer characteristics of both precise machine tool motions and tool profiles into workpieces to achieve submicrometer form accuracy and nanometer surface finishing. The cutting force is a key physical parameter for process plan and process monitor, since it directly affects the heat generation, machining quality, and tool life during machining [3]. Therefore, a lot of cutting force prediction models has been established by considering different influencing factors in static cutting process [4], such as machining parameters, cutter geometry [5, 6], workpiece material properties [7], and tool wear [8]. In 1958, Tobias and Fishwick [9] presented the incremental

✉ Wenyan Tang
twysyb@gdut.edu.cn

¹ State Key Laboratory of Precision Electronic Manufacturing Technology and Equipment, Guangdong University of Technology, Guangzhou, China

² State Key Laboratory in Ultra-Precision Machining Technology, Department of Industrial and Systems Engineering, The Hong Kong Polytechnic University, Kowloon, Hong Kong

³ School of Electromechanical Engineering, Guangdong University of Technology, Guangzhou, China

variation of the chip thickness affecting cutting force and built the first analytical model of dynamic cutting force. After that, lots investigations were conducted to study the influences of chip thickness variation to develop dynamic cutting force models [10, 14]. Ling and Weng [15] pointed out that the variation of chip thickness and the periodic variation of shear angle were the main reasons for chatter occurring and developed a dynamic force model in orthogonal cutting by adding the shear angle oscillations with effects of wavy surface profile and tool vibration.

Dynamic cutting force model in macro-cutting process has been established by considering the incremental variation of the chip thickness, the shear angle oscillations with wavy surface profile effect and tool vibration effect, etc., but few studies are found in microcutting. The cutting mechanics in microscale range is limited by inherent physical process issues therefore cannot be simplified by scaling-down the understanding of conventional processes [16]. In the microrange of the unit material removal, some issues, such as the geometries of cutting tool edge [16], grain size [18], and microstructure of workpiece materials [19], are ignorable in conventional machining but become dominant factors on the cutting mechanics and surface generation in microcutting [20, 21]. It is well known that UPDC employs micrometer cutting parameters in its finishing process to achieve the required higher surface quality and larger cutting parameters employed in rough and half-finishing processes of UPDC to improve machining efficiency. Due to the microscale machining parameters in finishing process, the surface quality in UPDC is affected by tool path planning, machining parameters, tool geometry, and material properties as well as machine tool, environmental conditions [22]. It was reported that the material effects on surface generation in UPDC include plastic side flow and elastic recovery of materials [23–25] and crystal orientation [26]. Especially, the cutting parameters and the undeformed chip thickness (UCT) reach micrometer range and become comparable to the cutting tool-edge radius. This leads to a fundamentally

different cutting mechanism, chip formation and surface generation due to the well-established “the minimum chip thickness (MCT)” phenomena. This infers that the variation of cutting depth not only induces cutting force fluctuation but also changes the material removal mechanism therefore surface generation in UPDC.

At the same time, the being machined surface of finishing process in UPDC comes from the machined surface of half-finishing process. As mentioned, the cutting parameters of half-finishing are larger than those of finishing process which makes the achieved surface in half-finishing rougher than the sub-micrometer form accuracy and nanometer surface finishing in finishing process. This indicates that, for the finishing process in UPDC, the surface being machined is not perfectly smooth but contains microscale topographies. Especially, the value of peak-to-valley (PV) height of half-finishing usually reaches to micrometer range, which is comparable for the micrometer cutting depth of finishing process therefore is not negligible for the cutting process and surface generation.

Therefore, in this study, the effect of the microscale topography on cutting process and surface generation of finishing process in UPDC are investigated, including the instantaneous cutting depth, shear angle, and effective rake angle as well as cutting force and surface generation. Based on the variation of cutting depth and shear angle, the dynamic cutting force model and surface generation model for orthogonal diamond cutting process are built. Experiments are conducted to verify the developed models.

2 Definition of microwavy profile

Figure 1 presents the orthogonal diamond cutting model on the smooth surface. It is well known that the kinematic surface topography in UPDC depends on machining parameters, tool geometry, and tool paths while other influencing factors will distort the tool-edge and tool-nose profiles in

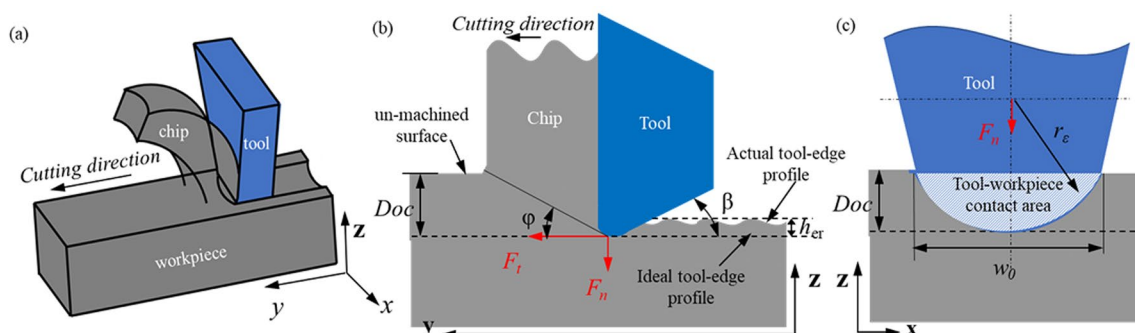


Fig. 1 a Orthogonal diamond cutting model on smooth surface and b tool-edge profile generation and c tool-nose profile generation in diamond cutting

UPC. From Fig. 1b, the theoretical tool-edge cutting profiles should be straight lines but become wavy curves due to the elastic and plastic deformations, while the tool-nose cutting profiles in UPC are the replications of the diamond tool nose on the machined surface, see Fig. 1c. For the smooth surface being machined, the depth of cut (Doc) keeps constant and is equal to the defined cutting depth. In this figure, r_ϵ and β refer to the nose radius and clearance angle of cutting tool, respectively. h_{er} is the elastic recovery height of the fresh generated surface and w_0 is the cutting width. However, from Fig. 2, the existence of microtopography on the surface being machined will induce variations of cutting depth (t_i) and shear angle (φ), since the shear angle varies in proportion to the slope of the upper surface of the workpiece being machined [27]. Referring to [15], the effect of microscale topography of surface being machined on finishing process in UPDC is name as microwavy profile effect in this study, which contains micrometer heights and pitches. Therefore, to study the cutting mechanism of UPDC under microwavy profile effect, the influence of microwavy profile on shear angle (φ), the instantaneous depth of cut (t_i), cutting force therefore surface generation in orthogonal diamond cutting are investigated, as shown in Fig. 2.

In Fig. 2a, the surface height ($Z_w(i), i = 1, 2, \dots, N$) of microwavy profile on the i th cutting point is represented as

$$Z_w(i) = A_w \left(1 - \left| \sin \left(\frac{\pi \cdot i \cdot \Delta l_p}{f_w} \right) \right| \right) \quad (1)$$

where Δl_p represents the horizontal distance of two adjacent discrete cutting points. A_w and f_w refer to the maximum height and the pitch of microwavy profile, respectively. For the finishing process of UPDC, f_w and A_w depend on the tool geometries and cutting parameters in half-finishing process.

Under the microwavy profile effect, as shown in Fig. 2b, c, the instantaneous depth of cut on the i th cutting point is the summation of the nominate depth of cut (t_0) and the microwavy profile height:

$$t(i) = t_0 + Z_w(i) \quad (2)$$

The actual contact area (S_f) between tool tip and workpiece also includes two parts: the static tool-workpiece contact area (S_0) and the wavy profile induced tool-workpiece contact area (S_w):

$$S_f(i) = S_w(i) + S_0(i) = \frac{\theta_i(i) \cdot \pi \cdot r_\epsilon^2}{360} - \frac{w(i)(r_\epsilon - Z_w(i) - t_0)}{2} \quad (3)$$

where $w(i)$ and $\theta_i(i)$ refer to the cutting width and center angle of the tool-workpiece contact area on the i th cutting point, respectively. $w(i) = \sqrt{r_\epsilon^2 - (r_\epsilon - t(i))^2}$, $\theta_i = 2 \cdot \arccos(w(i)/(2 \cdot r_\epsilon))$.

When the diamond tool nose in the cutting area is differentiated into a finite number (N_t) of tip differential elements (see Fig. 2c), each of them can be considered a single element being in an orthogonal cutting process. Consequently, under the wavy profile effect, the instantaneous cutting depth ($t(i, j)$, $i = 1, 2, N; j = 1, 2, \dots, N_t$) of the j th tool nose element on the i th cutting position is

$$t(i, j) = r_\epsilon \cos \alpha_0 - \frac{r_\epsilon \cos \alpha_0 - t_0 + A_w \left(1 - \left| \sin \left(\frac{\pi \cdot i \cdot \Delta l_p}{f_w} \right) \right| \right)}{\cos \left(\frac{\theta_r(i)}{2} - \frac{2 \cdot j \cdot \theta_r(i)}{N_t} \right)} \quad (4)$$

where α_0 is the nominated tool rake angle, which is usually equal to zero for a diamond cutting tool in ultra-precision cutting process: $\alpha_0 = 0$. The cutting width ($w(i, j)$) and tool-workpiece contact area ($S_f(i, j)$) of the j th tool nose element on the i th cutting position therefore can be represented as

$$\begin{cases} w(i, j) = \sqrt{r_\epsilon^2 - (r_\epsilon - t(i, j))^2} \\ S_f(i, j) = \frac{\theta_r(i, j) \pi r_\epsilon^2}{360} - \frac{w(i, j)(r_\epsilon - Z_w(i) - t_0)}{2} \end{cases} \quad (5)$$

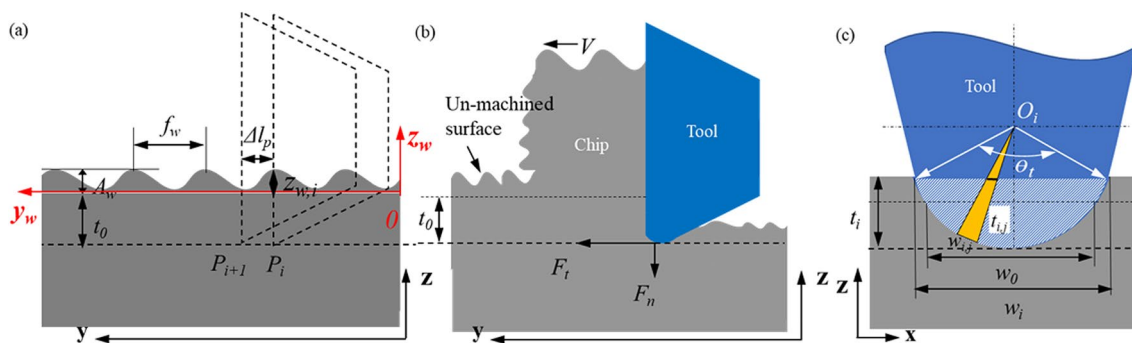


Fig. 2 a Definition of microwavy profile, b orthogonal diamond cutting model on microwavy profile, and c the instantaneous tool-workpiece contact area

3 Dynamic cutting model with wavy profile effect

3.1 Effective shear angle

From the above analyses, the wavy profile changes the depth of cut and tool-workpiece contact area, which are related to the material removal volume therefore affect the cutting process. Figure 3 presents the modified 2D cutting model for the j th tool tip differential element on the i th cutting

point to study the cutting process including the shear angle, the stress then to cutting forces and surface generation. It is noted that, although diamond cutting tool usually contains a zero rake angle, the tool rake angle in this section is positive. Moreover, considering the cutting edge radius of diamond tool is not negligible in ultra-precision cutting, the condition for a sharp cutting edge can be met by defining an equivalent rake face to form the linear interface between the lowest cutting point and the highest equivalent contact point [28] (see Fig. 3). The equivalent rake angle ($\alpha_e(i, j)$) is expressed as

$$\alpha_e(i, j) = \alpha_o + \left\{ \begin{array}{l} \tan^{-1} \frac{-r \cos \left[\sin^{-1} \left(\frac{\xi t(i, j)}{r} - 1 \right) \right]}{\xi t(i, j)}, \xi t(i, j) \leq r(1 + \sin \alpha_o) \\ \tan^{-1} \left[\frac{\xi t(i, j) - r(1 + \sin \alpha_o)}{\xi t(i, j)} \right] \cdot \tan \alpha_o - r \cos \alpha_o, \xi t(i, j) > r(1 + \sin \alpha_o) \end{array} \right\} \quad (6)$$

where r is the cutting-edge radius of diamond tool. ξ is a factor which determines the equivalent contact height between the tool and chip: $\xi \geq 1$ and $\xi t < l_{st}$ [29].

Moreover, since the actual cutting depth in ultra-precision cutting is much smaller than the tool nose radius, the material removal is modeled as plane strain deformation based on the planar strain plasticity theory [30]. For each tool tip differential element, the material is removed by shear-plastic flow if the actual instantaneous cutting depth ($t(i, j)$) is greater than the minimum chip thickness (h_{min}), that is, $t(i, j) > h_{min}$. Otherwise, the workpiece material cannot be removed and no chips are formed if $t(i, j) < h_{min}$.

To study the wavy profile effect on the actual depth of cut and the equivalent rake angle, simulation tests are conducted by defining the wavy profile is defined as $A_w = 1.8 \mu\text{m}$ and $f_w = 120 \mu\text{m}$. The nominate rake angle of diamond tool is 0° and its tool nose radius is 0.9865 mm . Cutting speed is 100 mm/min and the nominate depth of cut is $2 \mu\text{m}$: $F = 100 \text{ mm/min}$ and $t_o = 2 \mu\text{m}$. N_t is set as 100, which indicates that, in Fig. 2c, the tool nose involved in cutting process is differentiate into total 100 tool nose element: $j = 1, 2, \dots, 100$. The sampling frequency is set as 500 HZ; therefore the number of cutting points in one cycle of wavy profile is 36, that is, the total number of cutting points for three cycles in simulation is: $N = 108$. The 6th, 12th, 18th, and 24th cutting points

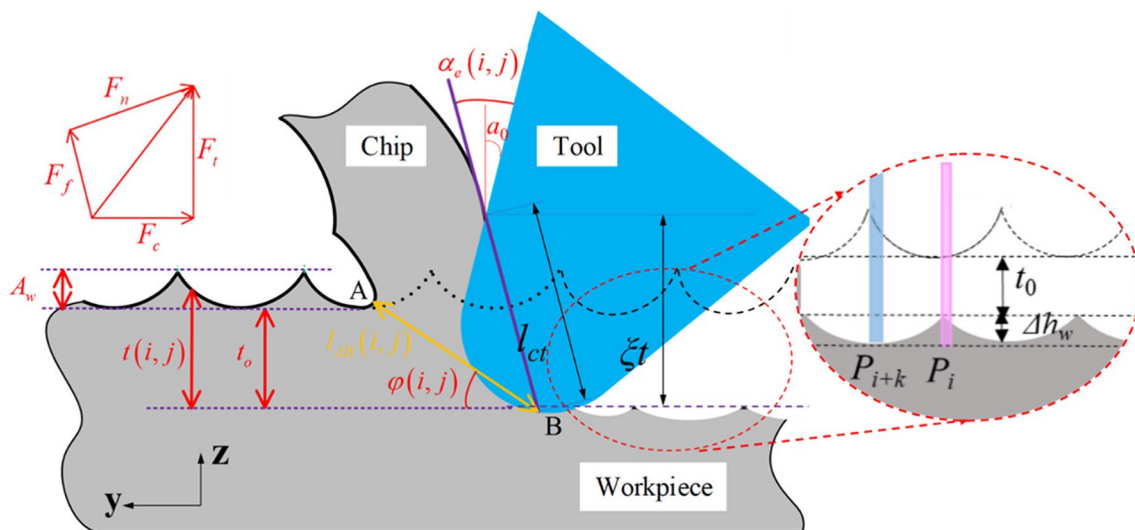


Fig. 3 Modified 2D cutting model of the j th tool tip differential element on the i th cutting point with wavy profile effect

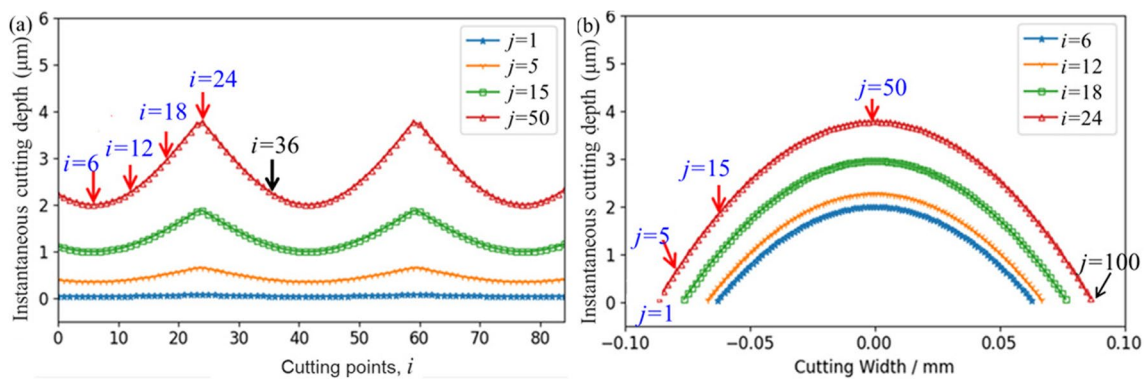


Fig. 4 Effect of wavy profile on the actual instantaneous cutting depth of **a** the 1st, 5th, 15th, and 50th tool tip differential elements along the cutting direction and **b** the 6th, 12th, 18th, and 24th cutting points on tool tip

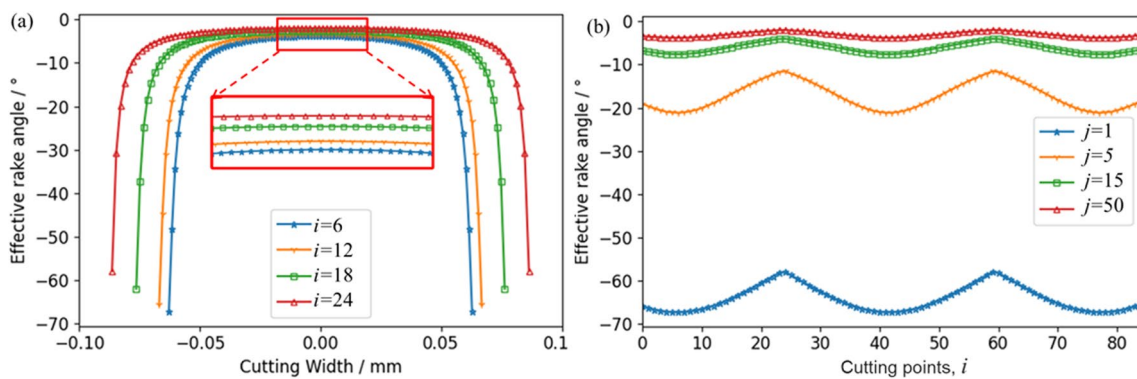


Fig. 5 The effect of wavy profile on effective rake angle of **a** the 1st, 5th, 15th, and 50th tool tip differential elements along the cutting direction and **b** the 6th, 12th, 18th, and 24th cutting points on tool tip

and the 1st, 5th, 15th, and 50th tool tip differential elements are selected to study the wavy profile effect on the actual depth of cut and the effective rake angle, as shown in Figs. 4 and 5.

From Fig. 4, along the cutting direction, the actual depth of cut of each tool tip element changes with the wavy profiles. Moreover, when the tool tip differential element is closer to the sides of the tool tip arc, the fluctuation of the actual cutting depth becomes smaller. As shown in Fig. 4a, the fluctuation extent of the 50th tip differential element (red curve in Fig. 4a) is much larger than the others. This indicates that wavy profile makes larger effect on the cutting depth of tool tip differential element closer to the tool tip center. Meanwhile, the cutting depth of tool tip element increases from tool tip side to the center. As presented in Fig. 4(b), the cutting depth of the 50th tip element reaches to the maximum and is equal to the summation of the nominate Doc (t_0) and the wavy profile height (A_w). Especially, the 24th cutting point contains the largest cutting depth (Fig. 4a) and also the widest cutting width (Fig. 4b), due to its location on the peak of wavy profile.

From Fig. 5, all the effective rake angles of each tool tip elements at each cutting points are negative, which is due to the zero rake angle of diamond tool and the existence of cutting edge radius in diamond cutting. In Fig. 4b, the actual cutting depths of the tool tip elements close to the tool tip sides are extremely small (see the 1st and 5th tool tip elements), while in Fig. 5, these elements also contain larger negative effective rake angles. This indicates that the negative rake effect increases as the actual instantaneous cutting depth decreases. The reason is that, when the actual cutting depth is smaller than the minimum chip thickness, the material removal mechanism changes from shearing to ploughing.

3.2 Dynamic forces and stresses

To developing cutting force model, some basic conditions and assumptions are established in this study: (1) The shear is represented by a straight slip line in the center of the first deformation zone, and its direction coincides with the directions of the maximum shear strain rate and the maximum

shear stress [31]. (2) The shear strain, shear strain rate, and temperature are uniform along the shear plane [32]. (3) When the cutting conditions is changed, the corresponding instantaneous cutting force is equal to the value of the steady state under the same cutting conditions [33]. Therefore, in Fig. 3, the shear angle is defined as the angle between the shear plane and the cutting direction, which is related to the primary deformation zone and affects the length of shear plane ($l_{AB}(i,j)$): $l_{AB}(i,j) = t(i,j)/\sin\varphi(i,j)$. The shear angle ($\varphi(i,j)$) therefore is expressed as the function of the tool effective rake angle ($\alpha_e(i,j)$) and the cutting ratio ($r_c(i,j)$):

$$\varphi(i,j) = \tan^{-1} \left(\frac{\cos\alpha_e(i,j)}{\frac{1}{r_c(i,j)} - \sin\alpha_e(i,j)} \right) \tag{7}$$

where $r_c(i,j)$ is the ratio of the undeformed chip thickness to the depth of cut.

The normal shear force on the equivalent rake face can be represented as

$$F_n(i,j) = \int_0^{l_{ct}} w(i,j)\sigma_n(l_p) \cdot dl_p = k_n\sigma_B \frac{\cos(\alpha_e(i,j) - \varphi(i,j)) \cdot w(i)t_o}{\sin\varphi(i,j)} \tag{8}$$

where l_p is the distance from the current cutting point P on the equivalent rake face to the lowest point of the cutting edge. l_{ct} is the length of the contact area between chip and the effective rake face (Fig. 4): $l_{ct}(i,j) = 2t(i,j)\cos(\varphi(i,j) - \alpha_e)/\sin\varphi(i,j)$. k_n is an equivalent scaling factor. σ_B

is the hydrostatic pressure at the bottom (Point B in Fig. 3) of the primary deformation zone: $\sigma_B(i,j) = \sigma_A(i,j) - 2\tau_s \cdot n \cdot BC_{ox}\gamma_s^n / (\sqrt{3}A + B\gamma_s^n)$, in which, C_{ox} is the Oxley factor [34] and σ_A is the hydrostatic pressure on the surface (Point A in Fig. 3) in the deformation zone [32]: $\sigma_A(i,j) = \tau_s [1 + 2(\pi/4 - \varphi(i,j))]$. A , B , and C are the initial yield stress, the strain hardening modulus and the strain rate strengthening parameter of workpiece materials, respectively.

On the other hand, as mentioned before, when the actual depth of cut is less than the minimum cutting depth (h_{min}): $t(i,j) < h_{min}$, the material cannot be removed. Moreover, due to the cutting edge radius in UPC, the material under the cutting edge

will produce a ploughing effect and part of the materials is under elastic deformation. The ploughing force is generally modeled to be proportional to the interference volume (S_p) [36]. Therefore, under the wavy profile effect, the ploughing force can be represented as

$$\begin{cases} F_{c,p}(i,j) = \mu_p k_{int} w(i,j) S_p(i,j) \\ F_{t,p}(i,j) = k_{int} w(i,j) S_p(i,j) \end{cases} \tag{13}$$

where μ_p is ploughing friction coefficient, k_{int} is the proportion ratio, and $S_p(i,j)$ refers to the interference area of the j th tip element between tool and workpiece during ploughing:

$$S_p(i,j) = r_\epsilon^2 (\arccos(1 - t(i,j)/r) - 0.5 \sin 2(\arccos(1 - t(i,j)/r))) \tag{14}$$

Therefore, the main cutting force and thrust force on the i th cutting point can be confirmed as follows:

$$\sigma_s = [A + B\epsilon_s^n] [1 + C \ln(\dot{\epsilon}_s/\dot{\epsilon}_0)] [1 - ((T_s - T_0)/(T_m - T_0))^m]$$

$$\tau_s = \sigma_s/\sqrt{3}, \gamma_s = \sqrt{3}\epsilon_s.$$

Meanwhile, the tool-chip friction state can be divided into sticking and sliding. The first friction state is generated near to the lowest point of the tool cutting edge, in which the frictional stress caused by the sticking effect keeps constant. For the second one, the frictional stress is proportional to the normal stress. Referring to [35], the distribution of normal stress on the equivalent rake face from the lowest point of the cutting edge to the current point (P) is $\sigma_n(l_p) = \sigma_B(1 - (l_p/l_{ct})^a)$. Therefore, the friction stress of tool-chip interface can be represented as

$$\tau_f(l_p) = \begin{cases} \mu_e \sigma_B \left(1 - \left(\frac{l_p}{l_{ct}}\right)^a\right) & 0 \leq l_p \leq l_{st} \\ \mu_e \sigma_n(l_p) & l_{st} < l_p \leq l_{ct} \end{cases} \tag{9}$$

where μ_e is the friction coefficient of tool rake face. l_{st} is the adhesion length of the chip to the tool rake face.

Then, the friction force on the equivalent rake face is

$$\begin{aligned} F_f(i,j) &= \int_0^{l_{st}} \mu_e w \sigma_B (1 - 2^{-a}) dl_p + \int_{l_{st}}^{l_{ct}} \mu_e w \sigma_n(l_p) dl_p \\ &= k_f \mu_e \sigma_B \frac{\cos(\alpha_e(i,j) - \varphi(i,j)) w(i) t_o}{\sin\varphi(i,j)} \end{aligned} \tag{10}$$

where k_f refers to the equivalent scaling factor in relation to friction.

Therefore, the main cutting force (F_c) and the thrust force (F_t) of the j th tool tip differential element of the i th cutting point can be confirmed as

$$\begin{cases} F_c(i,j) = F_n(i,j)\cos\psi(i,j) + F_f(i,j)\sin\psi(i,j) \\ F_t(i,j) = F_f(i,j)\cos\psi(i,j) + F_n(i,j)\sin\psi(i,j) \end{cases} \tag{11}$$

where $\psi(i,j)$ is the equivalent contact angle which is the angle between equivalent rake face and the direction of the actual cutting depth:

$$\psi(i,j) = \begin{cases} \cos^{-1} \left(\frac{l_{ct}(i,j)}{2r} \right) & l_{ct}(i,j) \leq \frac{\sqrt{2r\cos\alpha_o}}{\sqrt{1-\sin\alpha_o}} \\ \sin^{-1} \left(\frac{r+r\sin\alpha_o}{l_{ct}} \right) - \alpha_o & l_{ct}(i,j) > \frac{\sqrt{2r\cos\alpha_o}}{\sqrt{1-\sin\alpha_o}} \end{cases} \tag{12}$$

$$\begin{cases} F_c(i) = \sum \{F_{c,i,j} | \forall t(i,j) > h_{\min}\} + \sum \{F_{c,p,i,j} | \forall t(i,j) \leq h_{\min}\} \\ F_r(i) = \sum \{F_{r,i,j} | \forall t(i,j) > h_{\min}\} + \sum \{F_{r,p,i,j} | \forall t(i,j) \leq h_{\min}\} \end{cases} \quad (15)$$

From the above analyses, the wavy profile on the unmachined surface affects the diamond cutting process: when the cutting points locate on the peak of the wavy profile, the tool-workpiece contact area is larger than that on the valley. Especially, during the cutting process, the tool-workpieces contact areas on different cutting positions change periodically with same frequency as the wavy profile. Therefore, the wavy profile also makes the total main cutting force and thrust forces fluctuating periodically with the same frequency of wavy profile, which also affects the surface generation in diamond cutting process. In the following section, the dynamic surface generation model is developed in this study under the consideration of wavy profile effect.

3.3 Dynamic surface generation

During material removal process, when the diamond tool contacts with the workpiece and starts to remove materials, tool-chip contact area contains friction force which makes chip flow upward (along +Z direction) and tool moving downward (along -Z direction), as shown in Fig. 3. Therefore, on the peak of wavy profile (on cutting point P_i), diamond tool encounters a larger friction force and the diamond tool “penetrates” deeper into the workpiece, see the red circle area in Fig. 3. On the contrary, when the cutting point (P_{i-k}) located on the valley of wavy profile, the diamond tool causes a smaller thrust force therefore a shallower profile on the machined surface. The fluctuation height of surface profile not only is affected by the wavy profile and wavy profile induced force fluctuation, but also related to the workpiece material properties. In this study,

the peak-to-valley height ($\Delta h_w(i)$) of surface profile is represented as

$$\Delta h_w(i) = k_w \frac{H}{E} S_w(i)^{n_w} \quad (16)$$

where H and E are the hardness and elastic module of workpiece materials, respectively. k_w and n_w are two factors which will be confirmed by experimental method in this study.

Therefore, the surface profile height ($d_t(i, j)$) of the j th tool nose unit on the i th cutting point under the influence of microwavy profile can be determined:

$$d_t(i, j) = Z_w(i) + t_o - r_\epsilon + \sqrt{r_\epsilon^e - \left(\frac{w_w}{2} \left(1 - \left| \sin \left(\frac{\pi \cdot j \Delta w}{w_w} \right) \right| \right) \right)^2} + \Delta h_w(i) \quad (17)$$

From Eq. (17), the fresh generated surface shows fluctuation when the instantaneous cutting position reaches the peak of the wavy profile; the depth of cut increases then both the main cutting force and the thrust force reaches the maximum value which will affect the surface generation by introducing profile fluctuation on the machined surface in diamond cutting process. Therefore, in the following parts, single-point diamond turning (SPDT) is investigated as one case with the wavy profile effect.

4 Microtopography effect on SPDT

In SPDT, the diamond tool rotates around the spindle and feeds along X-axis of the machine coordinate system and its surface topography pattern is shown in Fig. 6. It can be found that, for finishing process in SPDT, the microtopography on the workpiece being machined is produced from the half-finishing process. In the orthogonal cutting process, the cutting direction keeps constant, while the cutting direction of diamond tool in

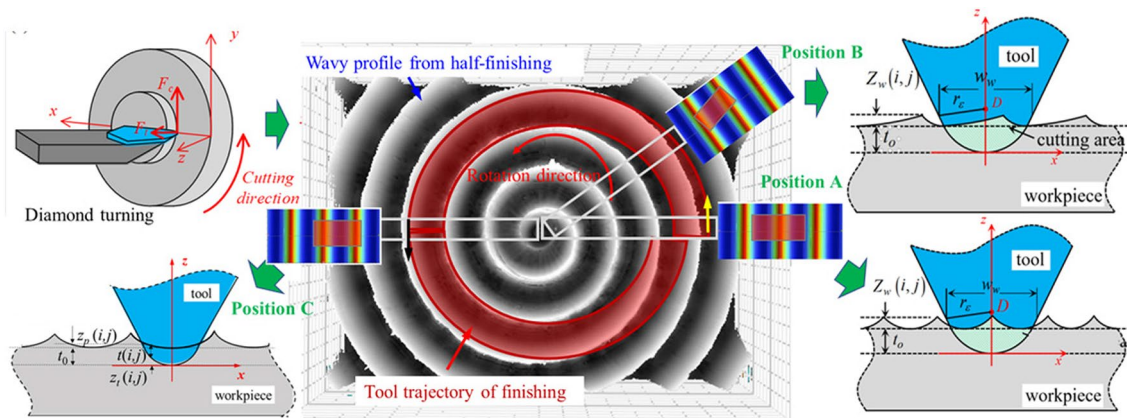


Fig. 6 Microtopography effect on finishing process in SPDT

SPDT changes instantaneously. Therefore, the microtopography in SPDT not only affects the tool-edge cutting profile but also induces different patterns of tool-workpiece contact areas, as shown in Positions A, B, and C in Fig. 6.

Considering the microtopography pattern effect and zero rake angle of diamond tool in SPDT, the instantaneous cutting depth ($t(i, j)$) of the j th tool nose element on the i th cutting point can be expressed as

$$t(i, j) = t_o(j) + z_{w,p}(i, j) - z_t(i, j) \tag{18}$$

where $z_t(i, j)$ is the z -value of the j th tool nose unit on the i th cutting point: $z_t(i, j) = \sqrt{r_\epsilon^2 - w^2(i, j)}$ $i = 1, 2, \dots, N$ $j = 1, 2, \dots, N_t$. On the cutting direction, $z_t(i, j)$ changes with the local cutting positions and sometimes is asymmetric to z -axis, see Position B in Fig. 6. $z_{w,p}(i, j)$ refers to the local topography height of the j th tool tip element on the i th cutting point, which depends on the cutting conditions of half-finishing process in SPDT.

To build the wavy profile pattern in SPDT, the tool tip trajectory is discretized in the Polar coordinates system, as shown in Fig. 7. The polar coordinates of the k round of the i th cutting points $p^k(i)(\rho^k(i), \theta(i))$ can be calculated:

$$\begin{cases} \rho^k(i) = R_{wp} - k \cdot f_h - i \frac{f_h}{N^k} \\ \theta(i) = i \cdot \frac{2\pi}{N^k} \end{cases} \tag{19}$$

where R_{wp} is the radius of workpiece and f_h is the feeding length per revolution of half-finishing process.

Since the tool tip trajectory rotates around the workpiece center and the instantaneous cutting direction of the tool is perpendicular to the polar diameter, the tool tip is discretized into N_t tool tip differential elements along the polar diameter

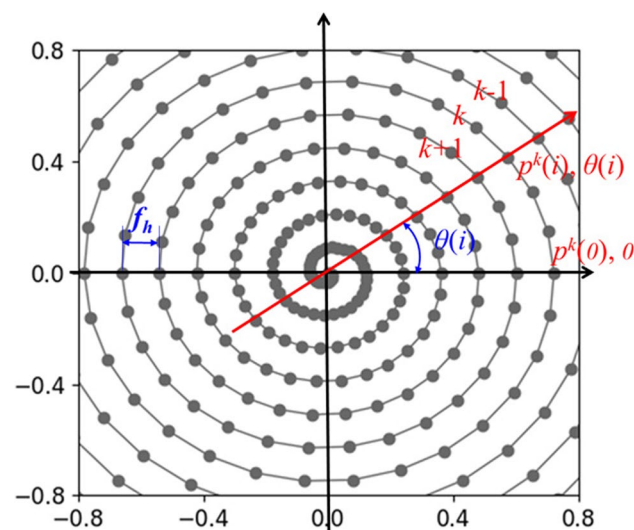


Fig. 7 Tool tip trajectory discretization of SPDT on polar coordinate system

direction. Then the polar coordinates ($\rho^k(i), \theta(i)$) and Z -value ($z_{w,t}^k(i, j)$) of the j th tool tip elements on the k th round and the i th cutting points are

$$\begin{cases} \rho^k(i, j) = R_{wp} - f_h \cdot \left(k + \frac{\theta(i)}{2\pi} \right) \\ z_{w,t}^k(i, j) = r_\epsilon - \sqrt{r_\epsilon^2 - \left(\rho^k(i, j) - \frac{w_\epsilon^k(i)}{2} + j \cdot \frac{w_\epsilon^k(i)}{N_t} - |\rho^k(i, j)| \right)^2} \end{cases} \tag{20}$$

And the Z -value of the point ($p(i, j) \theta(j)$) can be confirmed as

$$z_{w,p}(i, j) = \min \left\{ z_{w,t}^{k-2}(i, j), z_{w,t}^{k-1}(i, j), z_{w,t}^k(i, j), z_{w,t}^{k+1}(i, j), z_{w,t}^{k+2}(i, j) \right\} \tag{21}$$

Therefore, referring to Eqs. (18) to (21), the actual instantaneous cutting depth ($t(i, j)$) in the finishing process of SPDT can be calculated.

5 Experimental investigations

5.1 Nanoindentation test

As discussed before, under microwavy profile effect, the main cutting force and thrust force changes instantaneously with different cutting positions, which make the diamond cutting process being a dynamic process. To investigate the load on the surface generation, static and dynamic load are performed in nanoindentation tests for three materials including conventional aluminum alloy 6061-T6 (Al6061), rapidly solidified aluminum 6061 (RSA6061), and pure copper (copper).

To evaluate the hardness and elastic module of three materials, tests are conducted with 6 times by applying static load (15 mN) and holding for 10 s on cylinder samples (diameter 20 mm and height 25 mm). Table 1 lists the average values of the maximum indentation depths, hardness, and elastic module of 6 tests. It shows that hardness of two aluminum alloys is close and Al6061 contains a relatively higher elastic module. Moreover, copper contains the highest hardness among the three materials, which indicates that the higher the hardness, the smaller the indentation depth under the same load.

Table 1 Nanoindentation test results of three materials under 15 mN

	Maximum depth (nm)	Hardness (H, GPa)	Elastic module (E, GPa)	Ratio (H/E)
Al6061	585.42	1.585	94.694	0.01674
RSA6061	590.51	1.571	88.203	0.01781
Copper	553.71	1.677	146.363	0.01146

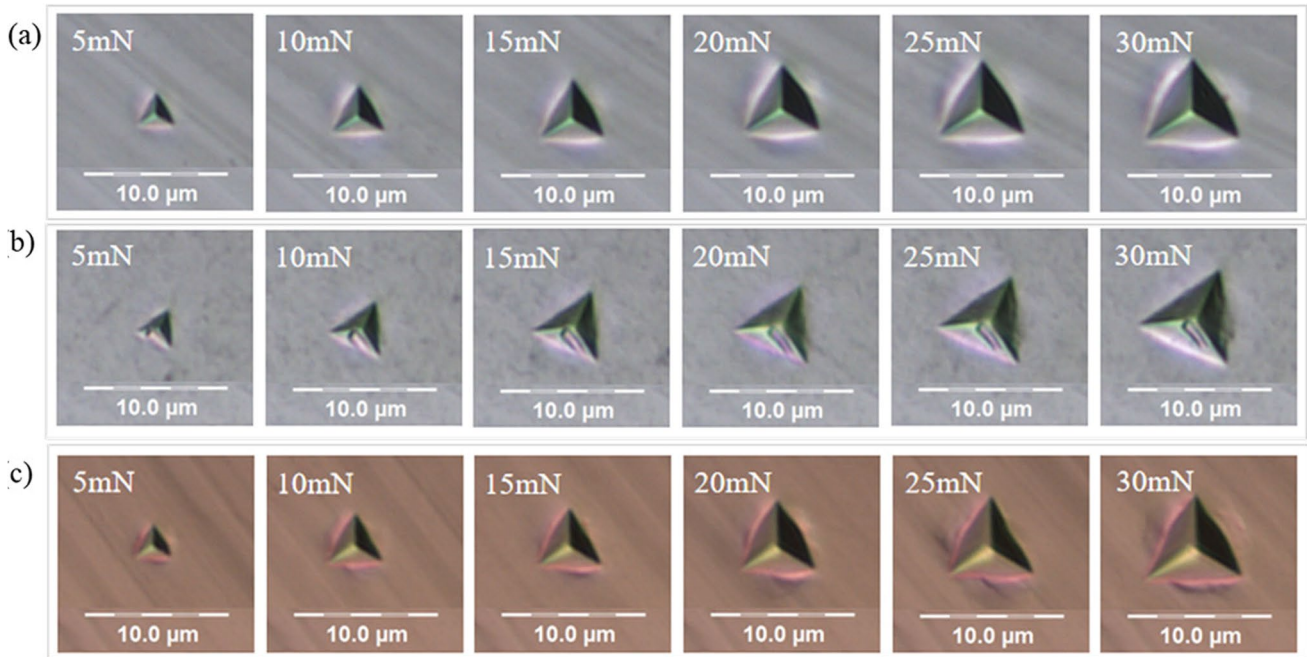


Fig. 8 The optical images of three materials under different loads: **a** Al6061, **b** RSA6061, **c** copper

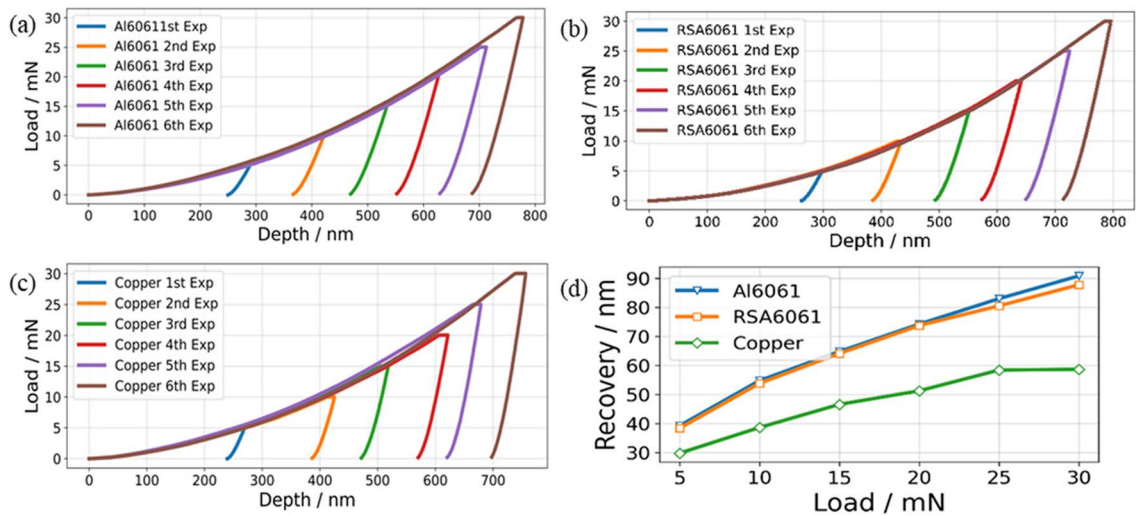


Fig. 9 The load-depth curves of three materials under different loads: **a** Al6061, **b** RSA6061, **c** copper, and **d** comparisons of elastic recovery height among three materials under different loads

Meanwhile, different values of loads ranging from 5 to 30 mN with interval of 5 mN are applied in nanoindentation experiment. As shown in Fig. 8, six tests are conducted on each material under different loads. Figure 9a–c shows the load-depth curves of six tests for each material. It should be noted that the loads applied in nanoindentation test are comparable with the thrust forces in diamond cutting process

under micrometer depth of cut. From Figs. 8 and 9, under different loads, the generated surface profiles of three materials are different; especially a larger load induces deeper profile.

During test, when the load-depth curve reaches to the maximum indentation depth, after 10 s holding time then beginning unloading, the indentation depth will gradually

decrease to a certain depth. This is due to the existence of material elastic recovery. Therefore, the difference between the maximum indentation depth and the remainder depth after completely unloading is used to evaluate the elastic recovery of the workpiece materials (see Fig. 9d). It can be found that, for the same materials, a larger load generates a higher recovery. Moreover, the elastic recoveries of two aluminum alloys are similar but both of them are larger than that of copper. Referring to Table 1, the materials elastic recovery depends on the ratio of hardness to elastic module (H/E): the smaller the ratio (H/E), the lower the recovery. And this also infers that the material with a higher ratio (H/E) will be more sensitive for the change of load, and the effect of force/load on surface generation will be more significant.

5.2 Determination of factors (k_w and n_w) for dynamic surface generation model

To study the wavy profile effect on surface generation in diamond cutting and confirm the two factors (k_w and n_w) in Eq. (16), diamond cutting experiments are conducted on ultra-precision machine (Moore Nanotech 350FG) with a diamond tool ($r_\epsilon = 2.06$ mm, $r = 207$ nm). The workpiece material is Al6061. The experiments are scheduled as follows:

- (1) Rough machining: diamond turning is conducted to achieve a flat surface on the machine system.
- (2) Half-finishing: microgrooving is performed by feeding along Y -axis (machine system) with depth of cut

Fig. 10 Strategy design for machining and measurement

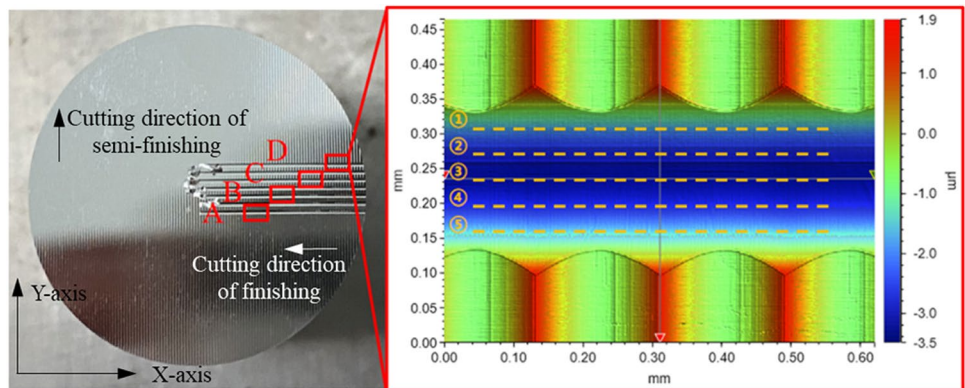
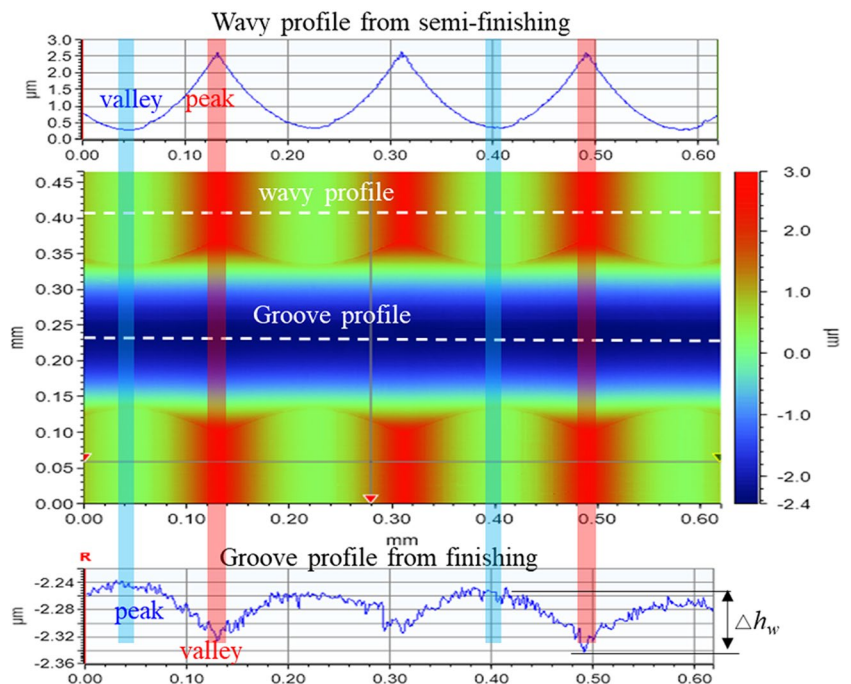


Fig. 11 Effect of wavy profile on cutting profile in diamond cutting (Position 3 in Area D)



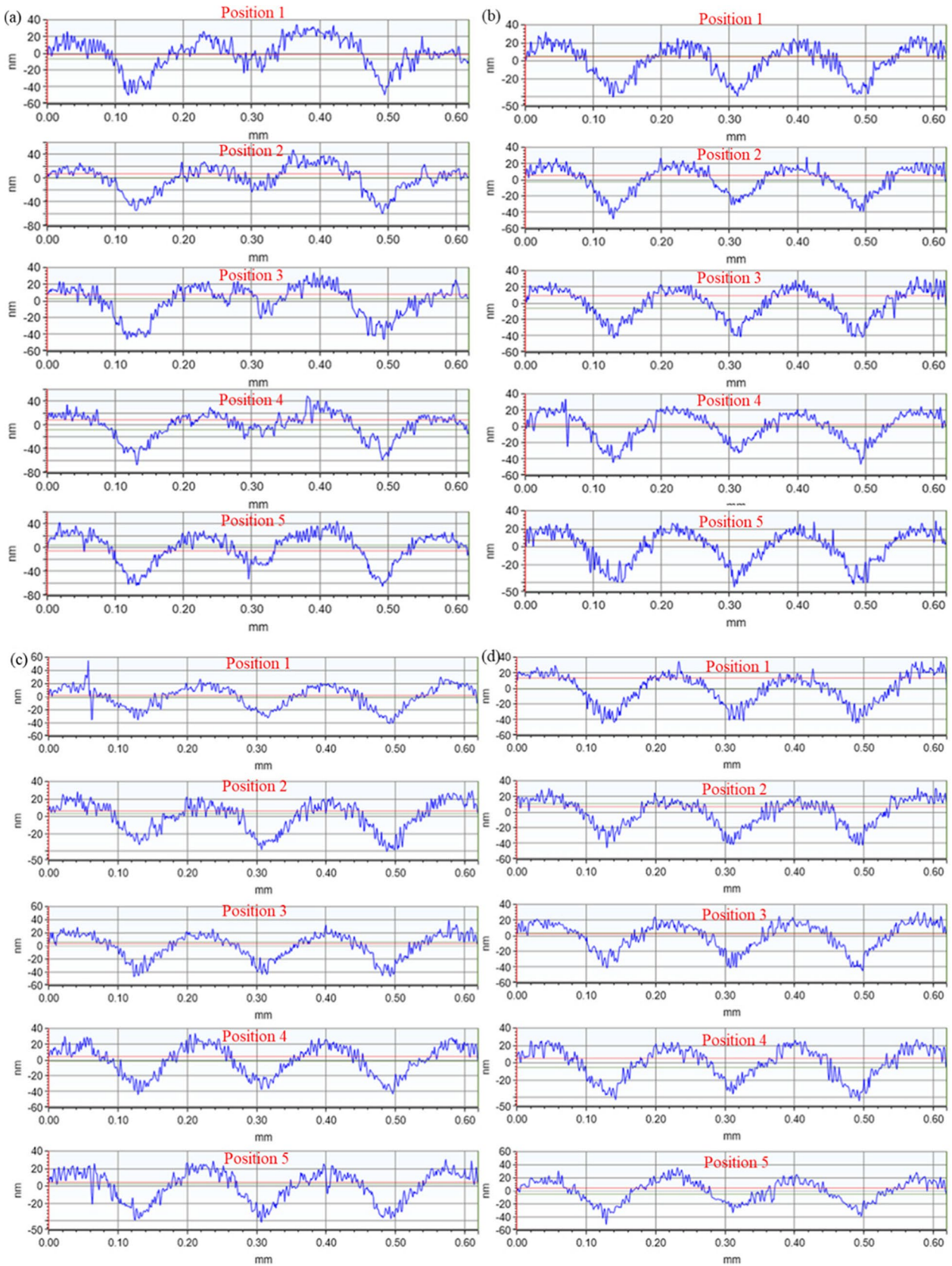


Fig. 12 The measured cutting profiles of five positions in different areas: a Area A, b Area B, c Areas C and d Area D

Table 2 Cutting parameters for the fabrication of four wavy profile patterns in half-finishing

Wavy profile pattern No	Feed rate, F (mm/min)	Spindle speed (rev/min)	Depth of cut (μm)	Step size, f_w (μm)	Theoretical wavy profile height, A_w (μm)
A	2	2000	3	\	\
B	500	\	3	60	0.22
C	500	\	3	180	1.97
D	500	\	3	240	3

3 μm , feed rate 500 mm/min, and step size 3 μm to achieve wavy profiles on the whole machined surface (see Fig. 10).

- (3) Finishing: microgrooving is used by feeding along X -axis with depth of cut 3 μm , step size 0.5 mm, and feed rate 500 mm/min. There are total seven grooves in finishing process.

After machining, the sample is measured by an optical profiler (Bruker GT-X8) to evaluate the surface topography, as shown in Fig. 11. The generated wavy profile presents as microgroove structures with height ($A_w = 2.2 \mu\text{m}$) and pitch ($f_w = 180 \mu\text{m}$). The measurement and analysis processes are scheduled as follows:

- (1) Four areas are selected to measure the surface profiles on the seven grooves produced by finishing process (see Areas A, B, C, and D in Fig. 10). The locations of four areas are selected on Groove No. 1, No. 3, No. 5, and No. 7.
- (2) 2D cutting profiles along X -axis direction (cutting direction) are drawn from the 3D surface profiles of the measured areas, see the groove profile in Fig. 11. It can be found that, in the peak of wavy profile, the groove profile presents as valley while the groove profile is the peak on the valley of wavy profile. This agrees well with the previous theoretical analyses. The difference between the peak and valley of groove profile is the depth (Δh_w) of wavy profile induced surface profile fluctuation, as shown in Fig. 11.
- (3) Total five curves (2D cutting profiles along X -axis direction) are drawn from the measured area and the locations of five curves are shown in the right figure of Fig. 10. There are total 20 curves drawn from the measured 3D grooves and 640 points collected from each curves (see Fig. 12).
- (4) Referring to Eq. (3) to confirm S_w , then using the collected data in Fig. 12 and Eq. (16) to conduct polynomial fitting, and the factors (k_w, n_w) can be confirmed: $k_w = 17.096$ and $n_w = 0.8456$.

5.3 Model verification by orthogonal diamond cutting experiment

To verify the developed dynamic models of cutting force and surface generation with wavy profile effect, diamond cutting experiments are conducted on ultra-precision machine tools (Moore Nanotech 350FG) with three materials (Al6061, RSA6061, and copper). The diamond tool with nominate rake angle of 0° , clearance angle of 9° , tool nose radius of 2.06 mm, and tool-edge radius of 207 nm is used for half-finishing and finishing processes. The material properties have been characterized in the previous sections. The machining and measurement processes are similar with the previous experiment.

In half-finishing process, four patterns of microwavy profiles are generated on the machined surface. Diamond turning is conducted to produce Pattern A and microgrooving experiments are applied to generate Patterns B ~ D with different profile height (A_w) and pitch (f_w) by setting different step size, see Table 2. In finishing process, single groove is generated on the surface with four wavy profile patterns by applying the same cutting parameters (feed rate 100 mm/min and depth of cut 2 μm). The cutting force signals are also collected in finishing process and samples are examined by optical profiler.

Figure 13a–d presents the measured wavy profiles of Patterns A ~ D, and Fig. 13a1–d1 shows the measured groove profiles on different wavy profile patterns for Al6061. From the measured wavy profiles, there are no obvious machining marks on the machined surface of Pattern A, which therefore is indicated as the perfectly smooth surface in this study. On the contrary, the profile heights and pitches get higher and wider from Pattern B to Pattern C then Pattern D (see Fig. 16b–d). This agrees well with the experiment design in Table 2.

Based on the established cutting force model with wavy profile effect, the predicted cutting force and thrust force for the orthogonal diamond cutting of Al6061 are compared with the measured forces, as shown in Fig. 14. It can be found that the predicted results are close to the measured ones. This infers that, the force prediction model under the consideration of wavy profile effect is capable for the diamond cutting within micrometer material removal range. Moreover, the existence of wavy profile induce force fluctuations, especially the amplitude of cutting force (F_y in Fig. 14) fluctuation is higher than that of thrust force (F_z in Fig. 14). In Fig. 14c, the main cutting force fluctuates in the range of 0.4 ~ 0.8 N while the thrust force in the range of 0.05 ~ 0.15 N for the wavy profile Pattern C. This indicates

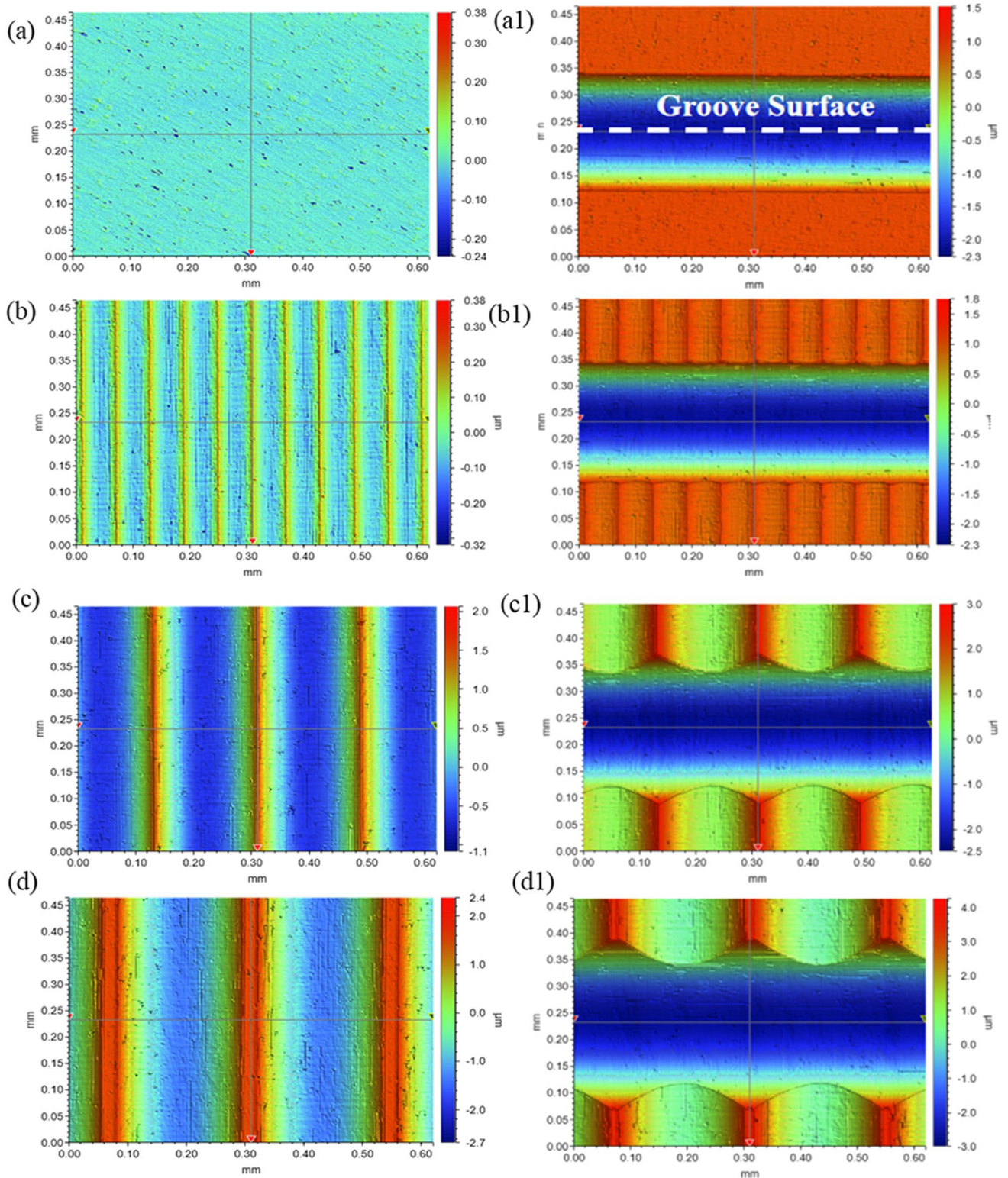
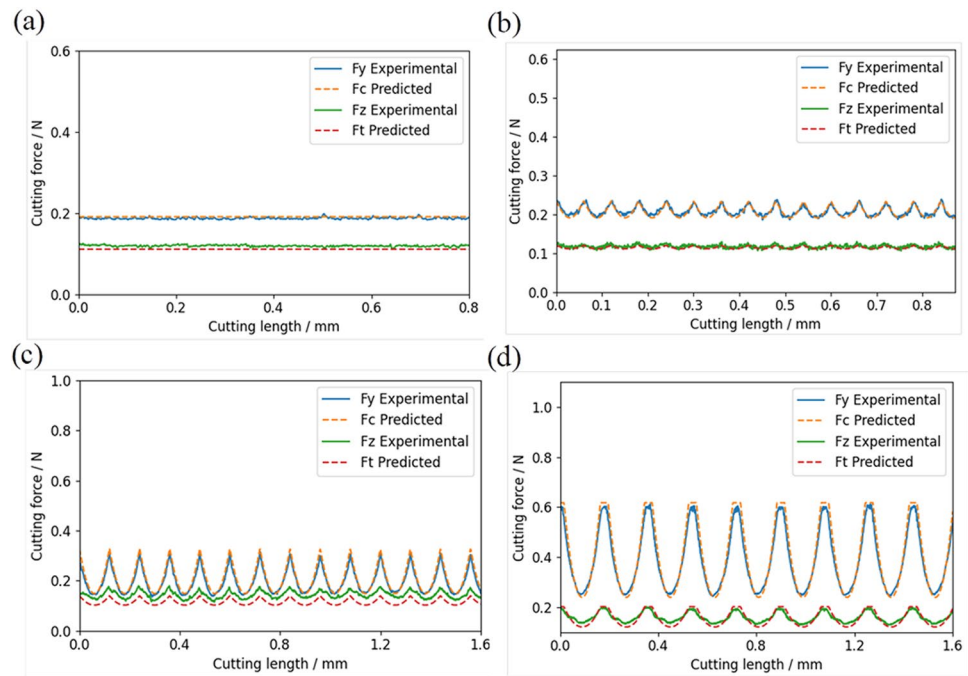


Fig. 13 The measured surface profiles of **a–d** wavy profile with different patterns and **a1–d1** groove surface on Al6061 with different patterns: **a**, **a1** Pattern A, **b**, **b1** Pattern B, **c**, **c1** Pattern C, and **d**, **d1** Pattern D

Fig. 14 Comparison between the prediction forces and experimental results on different wavy profile patterns in single cutting of Al6061: **a** Pattern A, **b** Pattern B, **c** Pattern C, and **d** Pattern D



that, the influence of wavy profile on cutting force is larger than that on thrust force. Meanwhile, by comparing the force signals of four wavy profile patterns, the amplitude of force profile increase with the wavy profile height and the frequency also becomes wider as wavy profile pitch gets larger.

To verify the surface profile prediction model in Eq. (16) and Eq. (17), 2D groove profiles in the cutting direction are drawn from the measured 3D groove profiles⁴, which are compared with the simulated surface profiles under wavy profile effect. Figure 15 presents the simulated and measured surface profiles of three materials under different wavy profile patterns. It shows that the simulated surface profiles agree well with the measured ones. Similarly with the cutting force profiles in Fig. 14, for the same workpiece materials, the higher the wavy profile height, the larger the PV values of 2D groove profiles, which also infer the more severe fluctuation of the generated surface microtopography in diamond cutting.

On the other hand, under the same cutting conditions, the same wavy profile pattern makes different effect on the cutting edge profile on different workpiece material; especially the wavy profile induced surface profile fluctuations of copper contain the smallest heights. From Fig. 15, for Pattern D, the wavy profile-induced PV heights of tool edge profiles on RSA6061, Al6061, and copper are 73.1 nm, 67.4 nm, and 46.5 nm, respectively. The reason is that copper contains the smallest ratio of hardness to elastic module (H/E) in Table 1 and the smallest recovery in Fig. 9d and, therefore, is the least sensitive to force change induced by

wavy profile, which also agrees well with the analyses in the nanoindentation test.

5.4 Single diamond turning experiment

To make a further study on the wavy profile effect in SPDT, diamond turning experiment is conducted on Al6061 with a single crystal diamond cutting tool (tool nose radius 0.9865 mm). The machining strategy is scheduled as follows: (1) Half-finishing: Diamond turning is conducted to generated the microwavy profile with spindle speed 2000 rpm, depth of cut 3 μm , and feed rate 240 mm/min. (2) Finishing: Diamond turning with zero feed rate is applied with depth of cut 2 μm and spindle speed 16 rpm, as shown in Fig. 16a. During machining, force signal is also collected, and the samples are also measured by optical profiler (see Fig. 16b).

In finishing, diamond tool rotates from cutting angle 0° (the green point in Fig. 15a) to 360° (the red point in Fig. 16a) and removes materials on the machined wavy surface from half-finishing. Figure 17a,b presents the simulated surface profile and the main cutting force in finishing process. It can be found that, under the wavy profile effect, the surface profile height, the tool-workpiece contact width and the main cutting force change with the local cutting position (different cutting angle in SPDT). From Fig. 17a, the generated surface profile slowly changes from nearly symmetric at 0° to asymmetric at 90° . After that, the cutting width begins to decrease from about 100° and surface profile slowly changes to symmetric with constant surface height

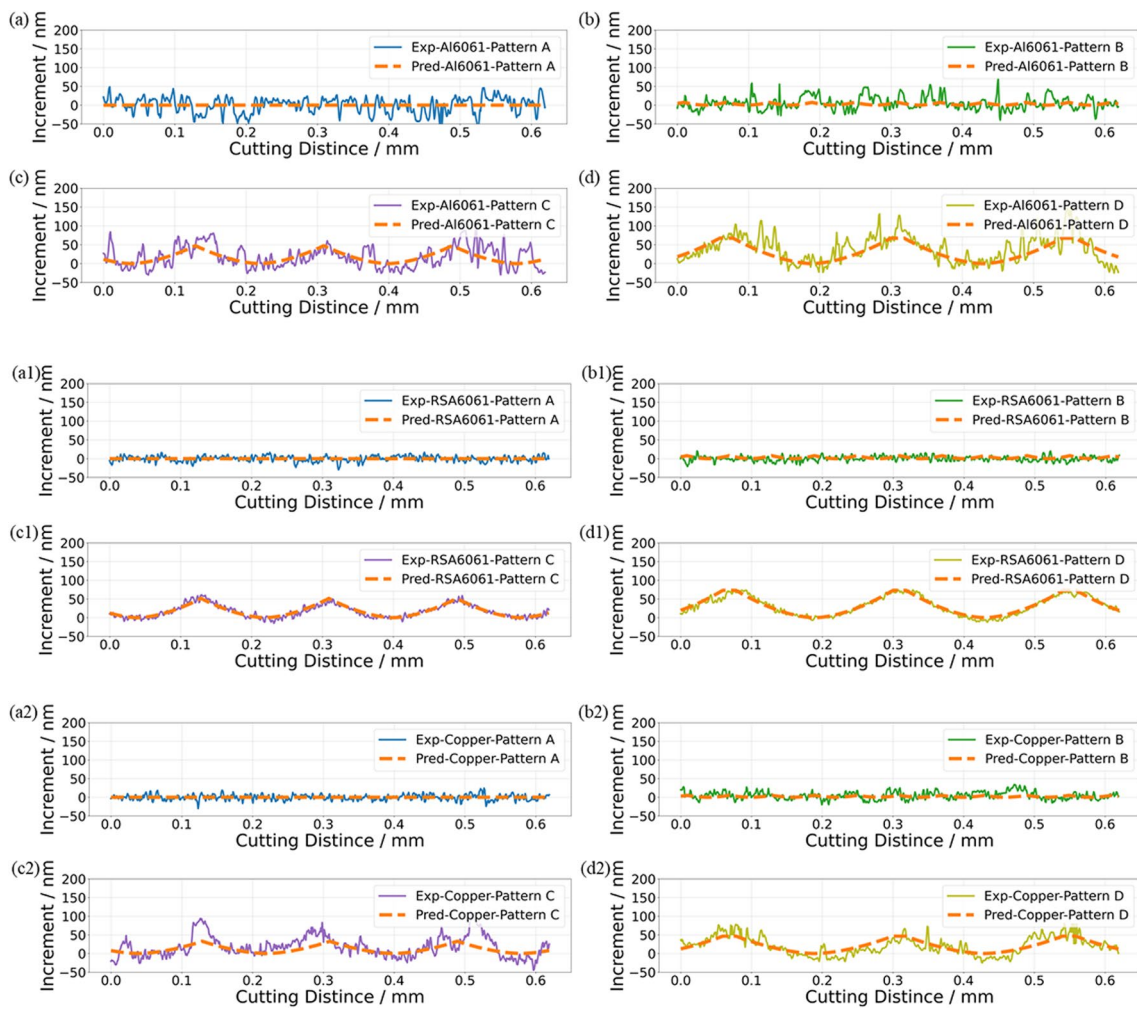
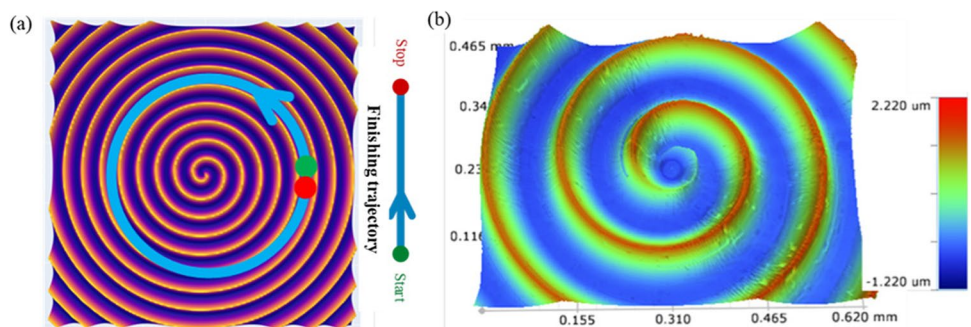


Fig. 15 Comparisons between predicted profiles and experimental results in diamond single cutting of different materials: **a–d** Al6061, **a1–d1** RSA6061, and **a2–d2** copper under different wavy profile patterns: **a** Pattern A, **b** Pattern B, **c** Pattern C, and **d** Pattern D

Fig. 16 a The designed wavy profile in half finishing and tool path planning in finishing and **b** the measured profile after half-finishing

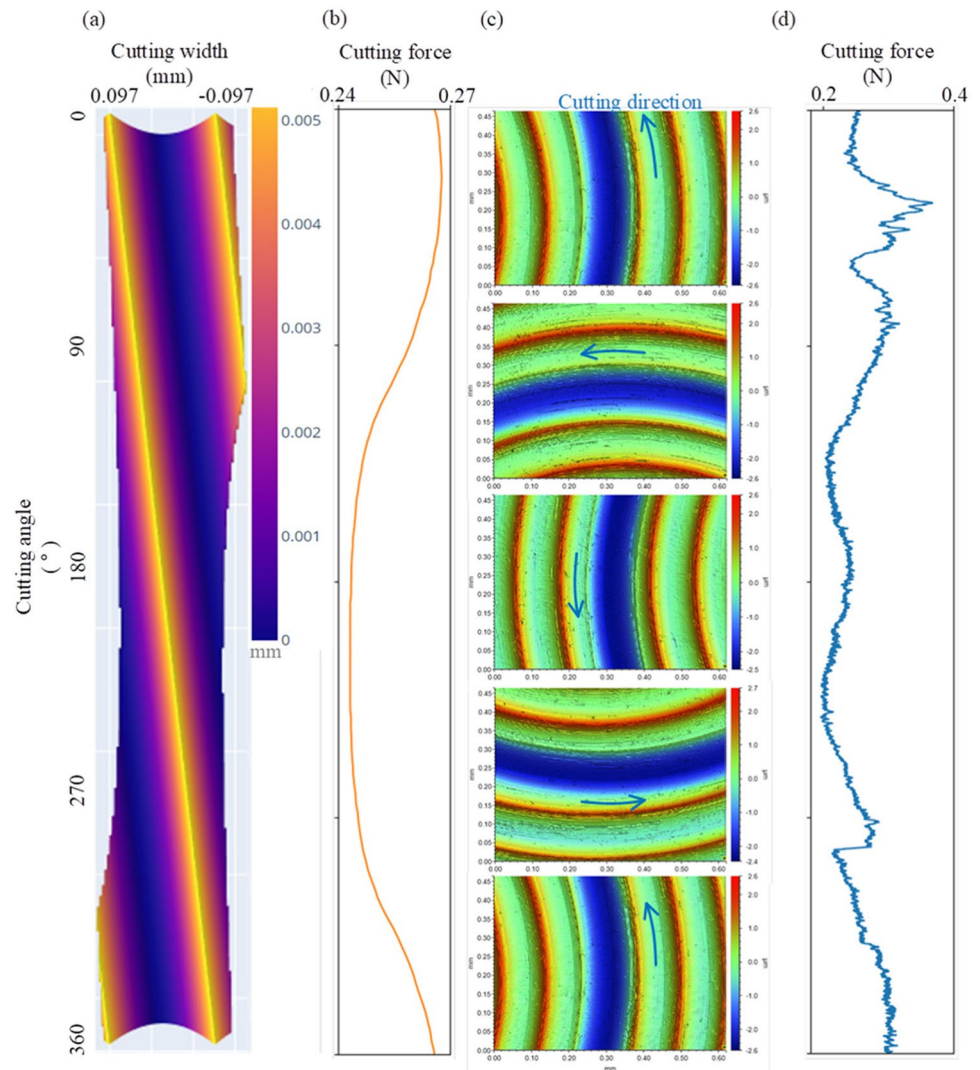


before 270°. Later, surface profile becomes asymmetric from 270 to 360°. This agrees well with the theoretical analyses for the wavy profile effect on surface profile in SPDT (see Fig). 6. Figure 17c presents five measured surface profiles at cutting angle 0°, 90°, 180°, 270°, and 360°, which are similar with the changes of the simulated profiles in Fig. 17a.

This infers that the dynamic surface generation model is capable for the prediction of surface profile in SPDT under microwavy profile effect.

Figure 17b presents the predicted main cutting force in finishing process. It shows that, the main cutting force firstly decreases slowly, then the downward trend increases due to

Fig. 17 Comparisons of simulated **a** surface profiles and **b** main cutting force with the measured **c** surface profiles, and **d** main cutting force in diamond turning of Al6061



the decreases of cutting width (see Fig. 17a). After that, the main cutting force becomes relatively stable between 100° and 270° , later slowly increases then rapidly increases after 290° due to the increase of cutting width. Figure 17d shows the measured main cutting force, which can be indicated that the main trend of the measured cutting force signal is similar with the simulated main cutting force.

6 Conclusion

This paper proposes dynamic models for cutting force and surface profile in ultra-precision diamond cutting (UPDC) by adding the effect of microway profile on cutting process and surface generation. The surface topography of half-finishing process is also considered on the finishing process to predict the cutting forces and surface profiles in single point diamond turning (SPDT). Diamond cutting and turning experiments are conducted to verify the developed models

and the predicted results meet well with the experimental results. The major findings are presented as follows:

- (1) The existence of microway profiles induces variation of instantaneous cutting depth and changes shear angle, stresses, and effective rake angle and therefore makes the main cutting force and thrust force fluctuating. Especially, the wavy profile effect on the main cutting force is larger than that on thrust force.
- (2) The force signal from the diamond cutting experiment agrees well with the predicted ones from the dynamic force model and both of them are similar with the microway profile. Moreover, the fluctuation extent of forces depends on the height of microway profile.
- (3) The microway profile also affects the surface generation in diamond cutting, however the generated surface profile shows completely opposite trend as compared with the microway profile. The reason is that, the peak

- of microwavy profile induces a larger thrust force therefore generates a deeper profile on the machined surface.
- (4) The microwavy profile effect on the generated surface profile is affected by the material properties: the higher the elastic recovery height, the more significant the wavy profile effect. Therefore, in the diamond cutting experiment, the fluctuations of the surface profile on copper are smaller than that of two aluminum alloys.
 - (5) Same with the microwavy profile effect on cutting force, the larger the height of microwavy profile is, the rougher the generated surface profile in diamond cutting becomes. Especially, as the wavy profile height is close to the cutting depth, the microwavy profile effect on cutting forces and surface generation is ignorable in UPDC.
 - (6) Different from orthogonal cutting, the microtopography pattern on the unmachined surface not only affects the turning forces and the tool-edge profile but also changes the tool-nose profile in diamond turning.

Author contribution All authors contributed to the manuscript preparation, experiment design, and data collection. Material preparation, experiment design, data collection, and analysis were performed by Lu Zhenghong, Hu Bowen, and Tang Wenyan. The final manuscript was finished by Wang Sujuan. The idea is provided by To Suet. All authors read and approved the final manuscript.

Funding The authors would like to express their sincere thanks to the support of the National Natural Science Foundation of China (no. 51975128 and no. 52005110).

Declarations

Competing interests The authors declare no competing interests.

References

1. Zhang S, Zhou Y, Zhang H et al (2019) Advances in ultra-precision machining of micro-structured functional surfaces and their typical applications. *Int J Mach Tool Manu* 142:16–41. <https://doi.org/10.1016/j.ijmactools.2019.04.009>
2. Ikawa N, Donaldson RR, Komanduri R et al (1991) Ultraprecision metal cutting—the past, the present and the future. *CIRP Ann* 40:587–594. [https://doi.org/10.1016/S0007-8506\(07\)61134-2](https://doi.org/10.1016/S0007-8506(07)61134-2)
3. Xu Y, Wan Z, Zou P, Huang W, Zhang G (2021) Experimental study on cutting force in ultrasonic vibration-assisted turning of 304 austenitic stainless steel. *Proc IMechE, Part B: J Eng Manuf* 235(3):494–513. <https://doi.org/10.1177/0954405420957127>
4. Wang S, Zhang T, Deng W et al (2022) Analytical modeling and prediction of cutting forces in orthogonal turning: a review. *Int J Adv Manuf Tech* 119(3):1407–1434. <https://doi.org/10.1007/s00170-021-08114-y>
5. Fang N, Dewhurst P (2005) Slip-line modeling of built-up edge formation in machining. *Int J Mech Sci* 47(7):1079–1098. <https://doi.org/10.1016/j.ijmecsci.2005.02.008>
6. Chen YH, Wang J, An QL (2021) Mechanisms and predictive force models for machining with rake face textured cutting tools under orthogonal cutting conditions. *Int J Mech Sci* 195:106246. <https://doi.org/10.1016/j.ijmecsci.2020.106246>
7. Adibi-Sedeh AH, Madhavan V, Bahr B (2003) Extension of Oxley's analysis of machining to use different material models. *J Manuf Sci Eng* 125(4):656–666. <https://doi.org/10.1115/1.1617287>
8. Li KM, Liang SY (2007) Modeling of cutting forces in near dry machining under tool wear effect. *Int J Mach Tool Manu* 47(7):1292–1301. <https://doi.org/10.1016/j.ijmactools.2006.08.017>
9. Tobias SA, Fishwick W (1958) Theory of regenerative machine tool chatter. *The Engineer* 205:199–203
10. Yan Y, Xu J, Wiercigroch M (2019) Modelling of regenerative and frictional cutting dynamics. *Int J Mech Sci* 156:86–93. <https://doi.org/10.1016/j.ijmecsci.2019.03.032>
11. Fodor G, Sykora HT, Bachrathy D (2020) Stochastic modeling of the cutting force in turning processes. *Int J Adv Manuf Tech* 111:213–226. <https://doi.org/10.1007/s00170-020-05877-8>
12. Lin SY, Chen CK (2010) Construction of a dynamic cutting force model for oblique cutting. *Proc IMechE, Part B: J Eng Manuf* 224(3):361–372. <https://doi.org/10.1243/09544054JEM1568>
13. Tarn YS, Young HT, Lee BY (1994) An analytical model of chatter vibration in metal cutting. *Int J Mach Tool Manu* 34(2):183–197. [https://doi.org/10.1016/0890-6955\(94\)90100-7](https://doi.org/10.1016/0890-6955(94)90100-7)
14. Li J, Yu W, An Q, Chen M (2020) A modeling and prediction method for plunge cutting force considering the small displacement of cutting layer. *Proc IMechE, Part B: J Eng Manuf* 234(11):1369–1378. <https://doi.org/10.1177/0954405420921739>
15. Lin JS, Weng CI (1990) A nonlinear dynamic model of cutting. *Int J Mach Tool Manu* 30(1):53–64. [https://doi.org/10.1016/0890-6955\(90\)90041-G](https://doi.org/10.1016/0890-6955(90)90041-G)
16. O'Toole L, Kang CW, Fang FZ (2021) Precision micro-milling process: state of the art. *Adv Manuf* 9:173–205. <https://doi.org/10.1007/s40436-020-00323-0>
17. Huang P, Lee WB (2016) Cutting force prediction for ultra-precision diamond turning by considering the effect of tool edge radius. *Int J Mach Tool Manu* 109:1–7. <https://doi.org/10.1016/j.ijmactools.2016.06.005>
18. Suarez Fernandez D, Jackson M, Crawforth P et al (2020) Using machining force feedback to quantify grain size in beta titanium. *Materialia* 13:100856. <https://doi.org/10.1016/j.mtla.2020.100856>
19. Zhao Z, To S, Zhu Z et al (2020) A theoretical and experimental investigation of cutting forces and spring back behaviour of Ti6Al4V alloy in ultraprecision machining of microgrooves. *Int J Mech Sci* 169:105315. <https://doi.org/10.1016/j.ijmecsci.2019.105315>
20. Cheng K, Huo D (2013) *Micro Cutting: Fundamentals and Applications*. John Wiley & Sons, Chichester
21. Zhang S, Zong WJ (2021) FE-SPH hybrid method to simulate the effect of tool inclination angle in oblique diamond cutting of KDP crystal. *Int J Mech Sci* 196:106271. <https://doi.org/10.1016/j.ijmecsci.2021.106271>
22. Zhang SJ, To S, Wang SJ et al (2015) A review of surface roughness generation in ultra-precision machining. *Int J Mach Tool Manu* 91:76–95. <https://doi.org/10.1016/j.ijmactools.2015.02.001>
23. Kong MC, Lee WB, Cheung CF, To S (2006) A study of materials swelling and recovery in single-point diamond turning of ductile materials. *J Mater Process Tech* 180(1–3):210–215. <https://doi.org/10.1016/j.jmatprotec.2006.06.006>
24. Zong WJ, Huang YH, Zhang YL et al (2014) Conservation law of surface roughness in single point diamond turning. *Int J Mach*

- Tool Manu 84(6):58–63. <https://doi.org/10.1016/j.ijmachtools.2014.04.006>
25. He CL, Zong WJ, Sun T (2016) Origins for the size effect of surface roughness in diamond turning. *Int J Mach Tool Manu* 106:22–42. <https://doi.org/10.1016/j.ijmachtools.2016.04.004>
 26. Cheung CF, To S, Lee WB (2002) Anisotropy of surface roughness in diamond turning of brittle single crystals. *Mater Manuf Process* 17(2):251–267. <https://doi.org/10.1081/AMP-120003533>
 27. Wallace PW, Andrew C (1965) Machining forces: some effects of tool vibration. *Int J Mech Sci* 7(2):152–162. https://doi.org/10.1243/JMES_JOUR_1965_007_023_02
 28. Vogler MP, Kapoor SG, Drvor RE (2005) On the Modeling and Analysis of Machining Performance in Micro-Endmilling, Part II: Cutting Force Prediction. *J Manuf Sci* 126:695–705. <https://doi.org/10.1115/1.1813471>
 29. Manjunathaiah J, Endres WJ (1999) A new model and analysis of orthogonal machining with an edge-radiused tool. *J Manuf Sci* 122(3):384–390. <https://doi.org/10.1115/1.1285886>
 30. Roth RN, Oxley PLB (1972) Slip-line field analysis for orthogonal machining based upon experimental flow fields. *J Mech Eng Sci* 14(2):85–97. https://doi.org/10.1243/JMES_JOUR/1972_014_015_02
 31. Oxley PLB, Hastings WF, Ford H (1977) Predicting the strain rate in the zone of intense shear in which the chip is formed in machining from the dynamic flow stress properties of the work material and the cutting conditions. *Proceedings of the Royal Society of London. A Math Phys Sci* 356(1686):395–410. <https://doi.org/10.1098/rspa.1977.0141>
 32. Li B, Hu Y, Wang X et al (2011) An analytical model of oblique cutting with application to end milling. *Mach Sci and Technol* 15(4):453–484. <https://doi.org/10.1080/10910344.2011.620920>
 33. Young HT, Mathew P, Oxley PLB (1994) Predicting cutting forces in face milling. *Int J Mach Tool Manu* 34(6):771–783. [https://doi.org/10.1016/0890-6955\(94\)90058-2](https://doi.org/10.1016/0890-6955(94)90058-2)
 34. Wang ZG, Rahman M, Wong YS et al (2005) A hybrid cutting force model for high-speed milling of titanium alloys. *CIRP Ann* 54(1):71–74. [https://doi.org/10.1016/S0007-8506\(07\)60052-3](https://doi.org/10.1016/S0007-8506(07)60052-3)
 35. Özel T, Zeren E (2005) A methodology to determine work material flow stress and tool-chip interfacial friction properties by using analysis of machining. *J Manuf Sci Eng* 128(1):119–129. <https://doi.org/10.1115/1.2118767>
 36. Germain D, Fromentin G, Poulachon G et al (2013) From large-scale to micromachining: a review of force prediction models. *J Manuf Process* 15(3):389–401. <https://doi.org/10.1016/j.jmapro.2013.02.006>

Publisher's Note Springer Nature remains neutral with regard to jurisdictional claims in published maps and institutional affiliations.

Springer Nature or its licensor (e.g. a society or other partner) holds exclusive rights to this article under a publishing agreement with the author(s) or other rightsholder(s); author self-archiving of the accepted manuscript version of this article is solely governed by the terms of such publishing agreement and applicable law.